ADVANCED ENERGY MATERIALS
www.advenergymat.de

Correlation of Band Bending and Ionic Losses in 1.68 eV Wide Band Gap Perovskite Solar Cells

Florian Scheler, Silvia Mariotti, Daniele Mantione, Sahil Shah, Dorothee Menzel, Hans Köbler, Maxim Simmonds, Thomas W. Gries, Jona Kurpiers, Viktor Škorjanc, Jinzhao Li, Amran Al-Ashouri, Philipp Wagner, Steven P. Harvey, Fengjiu Yang, Marin Rusu, Thomas Unold, Bernd Stannowski, Kai Zhu, Felix Lang, Dieter Neher, Eva Unger, Antonio Abate, David Mecerreyes, Martin Stolterfoht, Eike Köhnen, Lars Korte, Marko Topič, and Steve Albrecht**

Perovskite solar cells (PSCs) are promising for high-efficiency tandem applications, but their long-term stability, particularly due to ion migration, remains a challenge. Despite progress in stabilizing PSCs, they still fall short compared to mature technologies like silicon. This study explores how different piperazinium salt treatments using iodide, chloride, tosylate, and bistriflimide anions affect the energetics, carrier dynamics, and stability of 1.68 eV bandgap PSCs. Chloride-based treatments achieved the highest power conversion efficiency (21.5%) and open-circuit voltage (1.28 V), correlating with stronger band bending and n-type character at the surface. At the same time, they showed reduced long-term stability due to increased ionic losses. Tosylate-treated devices offered the best balance, retaining 96.4% efficiency after 1000 h (ISOS-LC-1I). These findings suggest that targeted surface treatments can enhance both efficiency and stability in PSCs.

1. Introduction

The efficiency gap between monocrystalline silicon and lead-halide perovskite single-junction solar cells is narrowing, with recent certified power conversion efficiencies (PCEs) of 27.3% and 26.7%, respectively, approaching the technologies' practical limits.[1–3] Additionally, silicon-perovskite tandem solar cells have reached a PCE of 34.6%.[3] Yet with a theoretical limit of ≈44%, there remains potential for further improvement.[4]

In tandem technology, the so-called "inverted" perovskite solar cell (PSC) stack (p-i-n) is predominant due to the higher transparency of n-type contact

F. Scheler, S. Mariotti, D. Menzel, H. Köbler, M. Simmonds, T. W. Gries, J. Kurpiers, V. Škorjanc, J. Li, A. Al-Ashouri, P. Wagner, M. Rusu, T. Unold, B. Stannowski, E. Unger, A. Abate, E. Köhnen, L. Korte, S. Albrecht
Solar Energy Division
Helmholtz-Zentrum Berlin
12489 Berlin, Germany
E-mail: steve.albrecht@helmholtz-berlin.de

F. Scheler, M. Topič
Faculty of Electrical Engineering
University of Ljubljana
Ljubljana 1000, Slovenia
E-mail: marko.Topic@fe.uni-lj.si

D. Mantione, D. Mecerreyes
POLYMAT
University of the Basque Country
Donostia-San Sebastián 20018, Spain

The ORCID identification number(s) for the author(s) of this article can be found under https://doi.org/10.1002/aenm.202404726

DOI: 10.1002/aenm.202404726

D. Mantione, D. Mecerreyes
Ikerbasque, Basque Foundation for Science
Bilbao 48013, Spain

S. Shah, F. Lang, D. Neher
Institute of Physics and Astronomy
University of Potsdam
14476 Potsdam, Germany

S. P. Harvey
Materials Science Center
Chemical and Computational Sciences (MCCS)
National Renewable Energy Laboratory
Golden, CO 80401, USA

F. Yang, K. Zhu
Chemistry and Nanoscience Center
National Renewable Energy Laboratory
Golden, CO 80401, USA

M. Stolterfoht
Electronic Engineering Department
The Chinese University of Hong Kong
Hong Kong SAR, China

S. Albrecht
Faculty of Electrical Engineering and Computer Science
Technical University Berlin
Marchstraße 23, 10587 Berlin, Germany

layers and low-temperature deposition processes.[5] In this configuration, recombination at the interface between the perovskite absorber and the fullerene C_{60} electron-selective material has been identified as a major bottleneck, limiting open-circuit voltage and thus PCE. This limitation has been attributed to: i) a high interfacial trap density near the lowest unoccupied molecular orbital (LUMO), resulting in Fermi-level pinning,[6,7] ii) charge-transfer states located in the middle of the perovskite's bandgap,[7] which could either be extrinsic defects or iii) virtual defect states formed by mixing of materials' wavefunctions[8,9] and iv) a LUMO to conduction-band (CB) offset.[10,11] This problem becomes more severe when increasing the bandgap from pure iodide lead perovskite with ≈ 1.5 eV[12] to wider bandgaps, where the conduction-band to LUMO (or to trap state) offset has been observed to further increase.[10,13,14] Various strategies have been employed to overcome these limitations, including chemical passivation (chemically reacting the surface to form a layer with less defects, reduce surface recombination or prevent further degradation), and selectivity enhancement by gradient doping (fixed charges inside absorber) or field effect passivation.[15] These strategies aim to reduce defect density and minority carrier density, effectively minimizing Shockley-Read-Hall recombination via traps. Recent record efficiencies in perovskite solar cells were achieved using surface treatments with diamine-related molecules (most recently in combination with others)[16,17] achieving a field effect like surface passivation.[11,16–18] Despite promising efficiencies, recent reports indicate a decrease in stability resulting from such post-treatments.[19] This can be seen as an outlier to the common observation that higher efficiencies correlate with greater stability,[20] yet the recent widespread use of diammonium salts in high-efficiency (wide-bandgap) devices underscores the need to address the lack of long-term stability in perovskite absorbers, particularly with focus on the interfaces.[21,22]

Stability protocols have been discussed and partially aligned both between research groups and in comparison to established protocols for other device types, but standard routines of maximum power point (MPP)-tracking under constant illumination fail to address the manifold observations specific to perovskite solar cells, many of which are linked to high densities of (shallow) mobile ionic defects.[23,24] Ion migration is linked to metastability phenomena (i.e., the temporal stability of non-equilibrium states) observed under varying illumination conditions.[25,26] Under operation conditions, mobile ions accumulate at the interfaces, which causes a redistribution of the electric field that normally acts as a driving force for charge extraction. The resulting interfacial charge accumulation causes PCE losses, mainly affecting short-circuit current density (J_{SC}) and fill factor (FF), which already shows in pristine devices.[19,27] With ageing, the ion density, and hence these "ionic losses", further increase, especially in the initial degradation-phase.[28] Although being partially recoverable in the dark, irreversible degradation processes eventually take over.[29,30] These processes are nucleated by heterogeneities in the form of phases or composition primarily at grain boundaries and interfaces, that can be the direct result of ion migration, and they manifest themselves as chemical reactions such as reduction-oxidation (redox), acid-base, or electrochemical reactions.[31–34] Eventually, permanent material loss occurs through the migration or out-diffusion of reaction products via grain boundaries into contact layers or the environment.[35,36]

Designing stable interfaces by passivating chemical defects and blocking irreversible chemical reactions and diffusion processes is thus crucial for obtaining stable devices.[37,38] Noteworthy examples in the literature demonstrate the effectiveness of combining different passivation approaches and diffusion-blocking layers. For instance, Zhao et al. used aluminium oxide to block unwanted reactions of their TiO_2 electron transporting layer (ETL), coupled with a 2D surface passivation of their all-inorganic perovskite, preventing reactions with the inorganic CuSCN hole transporting layer (HTL) and out-diffusion, eventually resulting in a projected stability of over five years.[39] Despite this and other promising examples,[40–43] a mechanistic understanding of the contribution of individual layers to degradation is often lacking, yet such understanding would contribute to designing more stable layer stacks. Especially for interfacial treatments, many results show benefits for both efficiency and stability.[18,44,45] In contrast, Caprioglio et. al. showed that in wide-bandgap perovskite absorbers, despite similar performance improvements resulting from either guanidinium bromide (GuABr) or imidazolium bromide (ImBr) interfacial treatments, the stability is reduced for the former while being increased for the latter.[14] They suggest that GuA^+ diffuses into the bulk perovskite more quickly due to its smaller size, accelerating the degradation process compared to the larger Imidazolium.

This example highlights the need for a deeper understanding of the molecular structure-to-function relationship, especially considering ion migration, which will aid in designing more stable interfaces and layers. We aim to contribute to this by investigating a model system of interfacial passivation, focusing on the influence of selected anions—iodide, chloride, tosylate (TsO), and bistriflimide (TFSI)—in state-of-the-art piperazinium salt surface treatments on the efficiency and stability of PSCs. We find a strong correlation between surface band bending, the surface dipole of the treated perovskite films (obtained via photoemission spectroscopy), and the open-circuit voltage, V_{OC}, of the final device, reflected in transient surface photovoltage (trSPV), transient photoluminescence (trPL), and photoluminescence quantum yield (PLQY) measurements. Chloride-based treatments achieve the highest efficiencies of 21.5% with V_{OC}s up to 1.28 V, which correlate with the strongest band bending near the C_{60} interface. We hence attribute the reduction of non-radiative recombination losses mainly to fixed positive charges at the interface, causing an accumulation of majority carriers (electrons) and reduction of minority carriers (holes), thus, an enhanced n-type character of the treated surface. Other passivation effects, for example reducing the defect density by chemical passivation, play a neglectable role for this perovskite composition and device-optimized surface treatments. Contrary to other reports and in line with more recent ones we observe an inverse correlation between PCE, governed primarily by the open-circuit voltage (V_{OC}), and long-term stability. Fast hysteresis (FH) measurements attribute the larger relative losses after ageing in higher efficient devices to reduced extraction, which is caused by accumulation of ions at the interfaces, and which is evident in reduced FF and J_{SC} values. Tosylate and bistriflimide-based treatments exhibit higher resilience to these losses with only a minor reduction in PCE (3.6% and 1.6%, respectively) after 1000 h

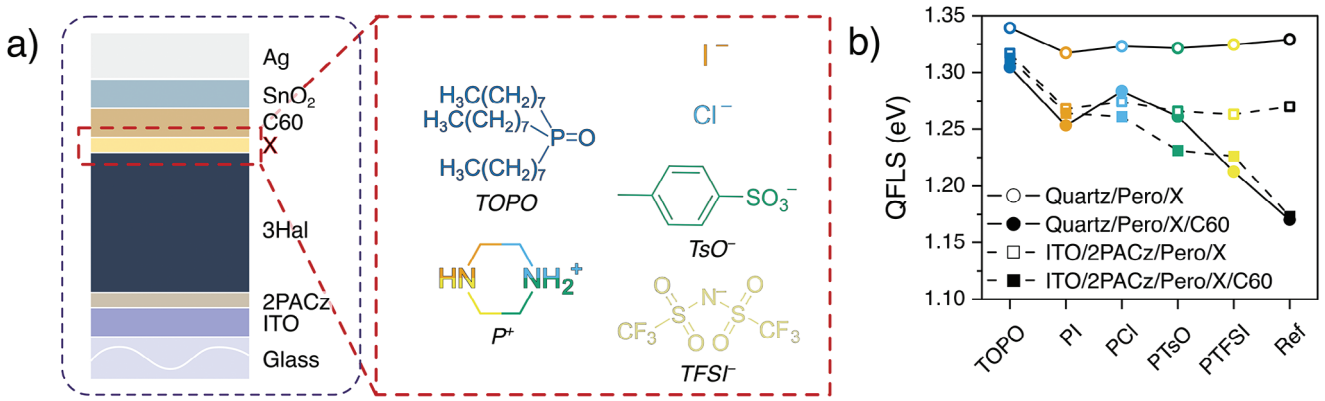

Figure 1. Influence of different layers and treatments on non-radiative recombination. a) Overview of the solar cell device stack employed in this study with the four salt combinations of piperazinium (P^+) with I^-, Cl^-, TsO^- and $TFSI^-$, which were used as interface modifiers between C_{60} and the perovskite depicted on the left. b) Quasi–Fermi-Level-Splitting of different half stacks with and without the different interfacial treatments. The half stacks consist of perovskite films coated on either quartz or glass/Indium Tin Oxide (ITO)/[2-(9H-Carbazol-9-yl)ethyl]phosphonic Acid (2PACz) substrates with and without C_{60} deposited on top. Trioctylphosphine oxide (TOPO) is used for comparison to an ideal chemical passivator, albeit featuring low charge extraction and conductivity. I^- = iodide, Cl^- = chloride, TsO^- = tosylate and $TFSI^-$ = bistriflimide.

under ISOS-L1 cycled conditions (N_2 ambient, 25 °C). We thus highlight the importance of addressing ion migration to overcome the stability limitations in perovskite photovoltaics, which are observed especially in the early degradation phase.

2. Results

We adopted a surface treatment based on piperazinium iodide (PI) previously used to reach 32.5% PCE in perovskite-silicon tandem solar cells, marking a former efficiency record in the year 2022.[11] The observed reduced recombination has been attributed to a combination of surface dipole and electron selectivity enhancement, reducing the energetic offset to C_{60} and preventing cross-interface recombination of minority carriers (holes) in the perovskite with electrons in the C_{60}. To investigate the impact of the anion for this surface treatment, a smaller, more electronegative, and less basic anion, chloride (Cl^-), and two larger ones, one with higher basicity, tosylate (TsO^-), and lower basicity, bistriflimide ($TFSI^-$), were selected. The structures are shown in **Figure 1**a. Trioctylphopsphine oxide (TOPO) is additionally listed, serving as a standard in several measurements for its known excellent chemical passivation properties, while not being applicable in full devices due to its insulating nature.[46] Figure 1a further shows the standard stack used for solar cell devices and for different characterization methods, comprising a glass/indium tin oxide (ITO) substrate, a hole transporting material consisting of self-assembled monolayer (SAM) 2PACz ([2-(9*H*-Carbazol-9-yl)ethyl]phosphonic Acid), a triple halide perovskite absorber with composition $Cs_{0.22}FA_{0.78}Pb(I_{0.85}Br_{0.15})_3$ + 5% $MAPbCl_3$, 1.68 eV bandgap energy and good phase stability first introduced by Xu et al.,[47] fullerene C_{60} electron transporting material combined with a tin oxide buffer layer and silver electrode. The treated perovskites surface layer using the respective target molecule will in the following be denoted as "X". Details about the fabrication can be found in the supporting information.

Figure 1b shows the Quasi–Fermi level splitting (QFLS) derived from absolute photoluminescence measurements (Figure S1, Supporting Information) on device stacks without (Ref) and with the different surface treatments as indicated. The perovskite absorber on a quartz substrate can reach a QFLS of 1.33 eV with a PLQY of 12.3%, further increasing up to 18.1% and 1.34 eV using TOPO passivation, demonstrating the high quality of the absorber bulk and the upper limit for implied V_{OC} values in best-passivated devices. Piperazinium-based surface treatments of quartz/perovskite films show a slight negative impact on the QFLS, indicating that the optimized concentrations do not effectively serve as chemical passivation for the perovskite composition used.[11] We observe an increase in PL emission, which suggests chemical passivation, but only at higher PCl concentrations (Figure S2a, Supporting Information). This is consistent with previous findings for wider bandgap perovskite absorbers.[48] Fourier transform photocurrent spectroscopy (FTPS) measurements in full devices further confirm that there is no significant reduction in sub-bandgap defect density following piperazinium salt treatment (Figure S2b, Supporting Information). Switching to an ITO/2PACz substrate, the QFLS is further reduced by ≈50 meV, except for TOPO, remaining above 1.3 eV. The introduction of C_{60} on top of the reference perovskite film reduces the QFLS to 1.15 eV, both on quartz and ITO/2PACz substrates, due to recombination dominated by additional channels at the Perovskite/C_{60} interface.[7] The thick TOPO layer effectively blocks these channels, with little impact on the QFLS which stays above 1.3 eV. For the stack ITO/2PACz/Pero/X/C_{60}, the different surface treatment salts reduce the C_{60} induced losses to a different degree, following the trend PCl > PI > PTsO > PTFSI. As described in our previous work, we infer a working mechanism of these salts by: 1) a field-effect-like passivation, increasing the n-type character of the surface (i.e., a shift of the work function, WF, toward the conduction band, CB), due to electron donation of the diammonium cation,[18] together with 2) a surface dipole (i.e., the equal shift of work function, WF, and ionization energy, I*) improving the energy alignment.[11] Electron donation and dipole of the whole salt are a sum of the cation and anion individual contributions.[49] For example, basicity, resulting from electronegativity and size, is an indicator of the interaction strength with other ionic species, with the tendency of lower

basicity anions forming salts with smaller dissociation energies or, in different terms, lower interaction with the crystal lattice. Considering this and results from previous works,[49] the interaction strength with the surface would follow the order Cl^- >I^- >TsO^-, with the non-coordinating anion $TFSI^-$ expected to show no considerable interaction with the surface and TsO^- forming the most covalent bond (see Table S1, Supporting Information for anion properties). Chloride has the strongest electrostatic interaction with lead, due to its low polarizability and high electronegativity, resulting in the largest positive fix charge. Consequently, comparing different halides, chloride was demonstrated to show the strongest Fermi-level shift toward the conduction band.[50] A reduced hole (or minority carrier) density close to the ETL is in line with reduced interfacial recombination and aligns with the trends of the QFLS results.

To obtain more insight into the chemical interaction of the different salts with the perovskite absorber and the surface morphology, we performed grazing incidence wide-angle X-ray scattering (GIWAXS) measurements. **Figure 2a** shows the angle-integrated diffractograms at incidence angles of 0.15 and 2.00° (for 2D diffractograms see Figure S3, Supporting Information), with higher surface and bulk sensitivity, respectively. We see one new feature in treated films at 11.4° when using a logarithmic scale (linear scale Figure S4, Supporting Information), especially in the PCl sample. Further measurements with transient absorption (TA) (Figure S5, Supporting Information), PL, of the extinction, and XRD (Figure S6a–c, Supporting Information respectively) could not confirm the association with a low dimensional phase, which when comparing with literature, would also be expected at lower angles.[51] Hence, we attribute this peak to a polytype defect,[52] which could result from the higher sensitivity of chloride samples to the measurements in air. Overall, all samples feature broadened and shifted peaks for the surface-sensitive measurements, indicating a less oriented or strongly textured surface.[53–55] Also, in scanning electron microscopy (SEM) top views (Figure S7, Supporting Information), there is no indication of the presence of a morphological change, as one would expect, for example, upon the formation of a low-dimensional perovskite phase.[53] UVVIS and PL measurements further confirm this, with the only differences between the samples being subtle changes of the bandgap, by no more than 50 meV (Figure S8, Supporting Information).

We performed X-ray photoelectron spectroscopy (XPS) to find chemical signatures and investigate the molecules' chemical interaction with the surface (Figure 2b). Focusing on the fingerprints for piperazinium (N 1s, ≈403 eV for C-N^+-C / ≈401 eV for C-N-C), we confirm the presence of its ammonium group for all treated films, while in PTsO no additional component attributed to the amine group was necessary for a good fit. This might point toward differences in the protonation state of the piperazinium on the surface in dependence of the anion, which is in line with previous considerations on acidity. A clear sulfur signal (S 2p, ≈169 eV) could confirm the presence of TsO (S 2p, ≈169 eV), while neither sulfur nor fluorine (F 1s, ≈685 eV) was detected for TFSI. We further confirmed the absence of TFSI signatures expected in N 1s, C 1s, S 2p, and F 1s in samples using higher salt concentrations (Figure S9a, Supporting Information). The high dissociation of the TFSI anion due to its strong acidity may result in the easy desorption from the surface during annealing or under vacuum during the measurement, with the organic ligand remaining anchored to the surface.[56,57] Looking at the peak ratios relative to lead for the different perovskite components (Table S2, Supporting Information), we find a Cs depleted (except for TFSI, being enriched) and Br/Cl enriched surface for all treated films. The amount of piperazinium-based perovskite (piperazinium)PbI_4 (assumed 1D Dion Jacobson compound)[58,59] relative to lead, as well as Br/Pb and Cl/Pb ratios, follow the trend PCl >PI >PTsO ≈PTFSI >Reference, identical with the one of the QFLS values. Since the voltage can be adjusted with the piperazinium salt concentration,[11] and assuming the main working mechanism to be the change of the n-type character on the surface, a higher piperazinium incorporation fits to a stronger down-ward band bending on the surface. Similarly, a widening of the bandgap by higher chloride and bromide content could result in better energy alignment with the ETL and better hole blocking, depending on the exact shift of conduction and valence band, both being influenced by the halide composition.[60] Finally, in line with previous considerations on n-type character and localized positive charge at the interface, we find the largest shift of the Pb 4f signal to higher binding energies for chloride, followed by iodide, with no shift for $TFSI^-$ and a shift to lower binding energies for TsO^- (Figure S9b, Supporting Information).

To confirm the presence of TFSI anions, which could not directly be detected by XPS, we performed additional time-of-flight secondary ion mass spectrometry (ToF-SIMS) measurements, providing higher sensitivity. Additionally, the depth profiling enables to investigate the potential diffusion of the different species into the bulk. Figure 2c) shows the depth profile with positive polarity, with the topmost panel showing the approximate position in the device stack using the averaged signals of the different layer stacks (Figure S10a, Supporting Information: individual profiles). We selected mass-to-charge ratios (m/z) specific for the different possible ionization products from the different layers.[48] The signal of $C_6H_{11}N_2^+$ (m/z = 87.14), a representative for piperazinium, is slightly increased for all treatments at the interface between fullerene C_{60} and the perovskite, indicating no evident diffusion of the cation into the bulk. In the bottom panel, the presence of a signal at m/z = 284.81, as expected for Cs_2F^+ also suggests the presence of the TFSI anion at this interface. The difference in results from SIMS compared to XPS might result from the interface being initially buried in the SIMS samples, reducing the exposure of the treated surface to vacuum. Figure 2d shows the depth profile with negative polarity, again with the top panel indicating the position in the stack (individual profiles: Figure S10b, Supporting Information). Sulfur and fluoride anions (S^- and F^-) further confirm the presence of the anions at the interface. The anions chloride and iodide from the surface treatment cannot be detected effectively since Cl^- and I^- are also part of the perovskite composition, and they are not show a considerable enrichment on the surface in these measurements.

We continued to investigate the impact of the different surface treatments on the energetic band positions at the surface using high-sensitivity ultraviolet photoemission spectroscopy (UPS) with near-UV excitation. A schematic of the band line-ups is depicted in **Figure 3a**), as derived from the secondary electron cut-offs (UPS, excitation photon energy of 6.5 eV, Figure S11a, Supporting Information) and the valence band maxima (Constant

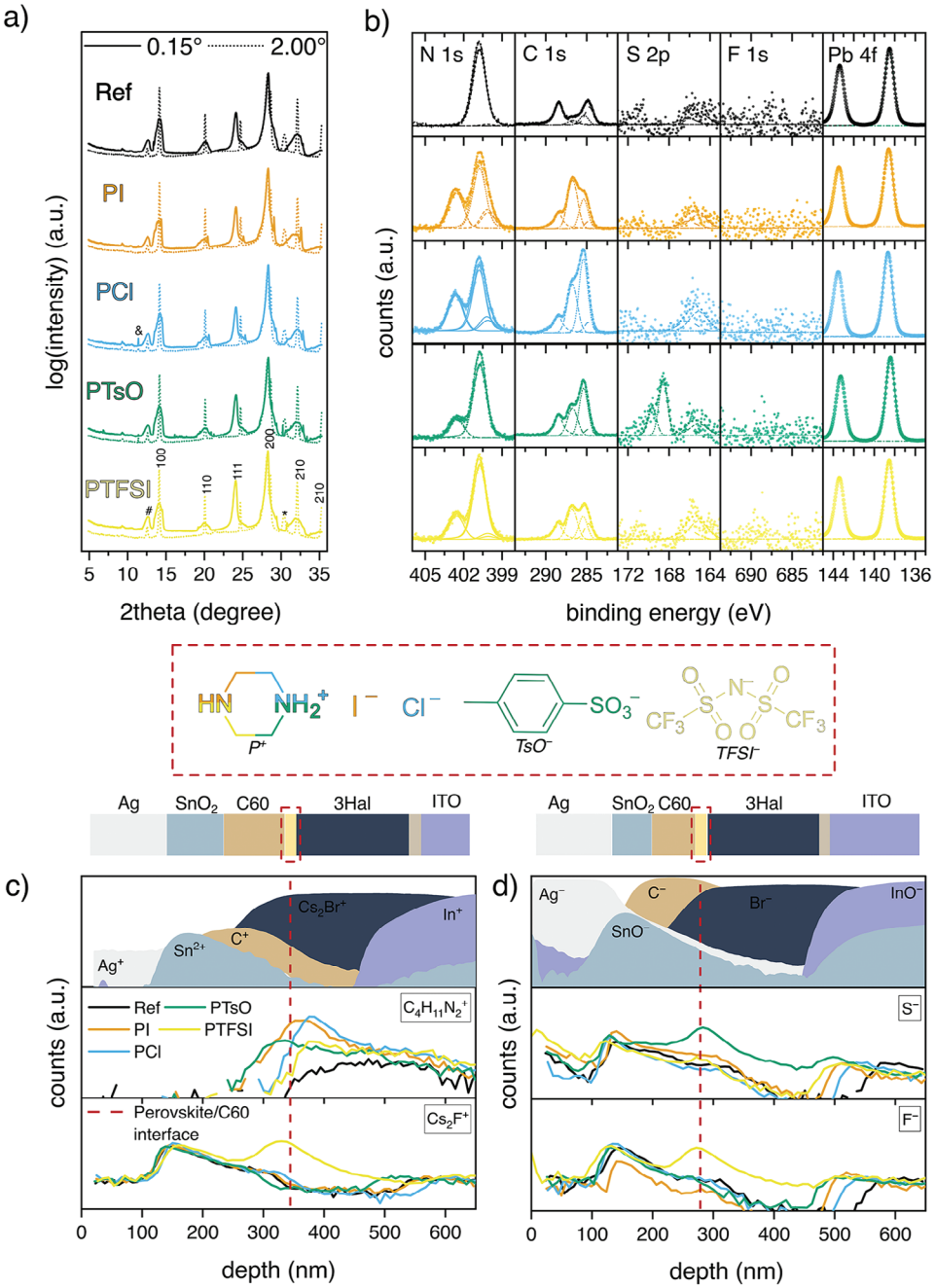

Figure 2. Surface chemistry and structural property changes resulting from interfacial treatments. a) XRD patterns of differently treated perovskite films on glass/ITO/2PACz substrates, recorded by using grazing-incidence wide-angle X-ray scattering (GIWAXS) at incident angles of 0.15° and 2.00°. '#', '*' and '&' indicate lead iodide, ITO and hexagonal defect phase, respectively. The perovskite 200 peak overlaps with the graphite 002 peak from the N_2- atmosphere measurement stage. b) N 1s, C 1s, F 1s, and S 2p core level features by X-ray photoelectron spectroscopy (XPS) of the same samples. Secondary ion mass spectrometry (SIMS) measurement results with positive (c) and negative (d) polarity on complete device stacks using the different surface treatments. Top panel: averaged depth profiles over the different samples showing selected species to indicate the position in the stack. Lower panels: count rate for mass ratios (m/z) assigned to fingerprint species from ionization of piperazininum (= $C_4H_{11}N_2^+$), bistriflimide (= $Cs2F^+$ / F^-), and tosylate (= S^-). The red dashed lines indicate the peak of fluoride, sulfide, and piperazine due to the presence of the passivation layer in the transition region between the C_{60} and perovskite layers.

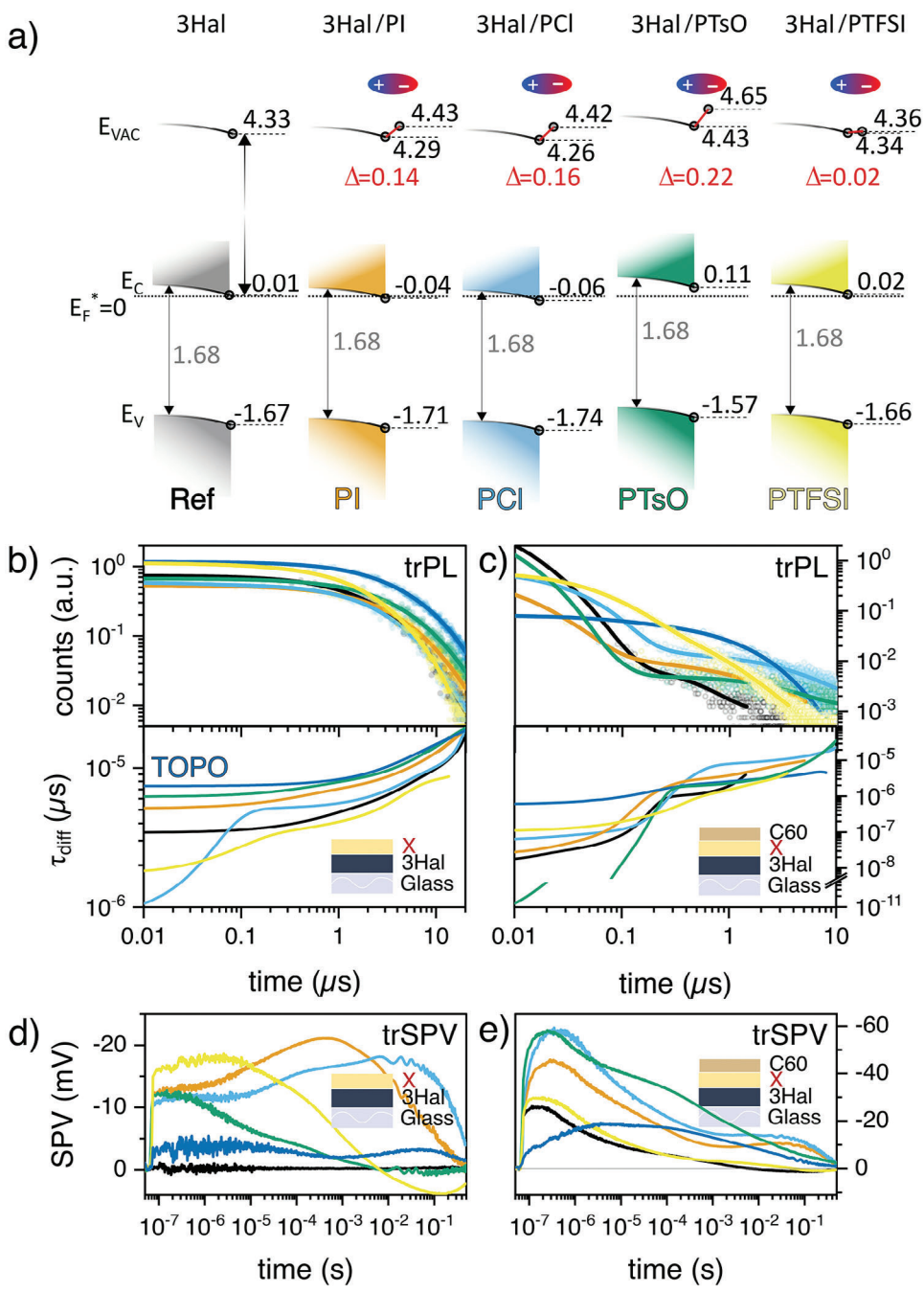

Figure 3. Energy levels and carrier dynamics with different interfacial treatments. a) Influence of the surface treatments on the vacuum level and band positions measured by ultraviolet photon spectroscopy (UPS). The measurements are referenced and aligned to the surface Fermi-Level being set to 0 eV (E_F*=0). The E_C (conduction band energy) is calculated relative to the E_V (valence band energy) using the perovskite's optical bandgap. For the precise determination of the work function (WF), an excitation energy of 6.5 eV was used. The ionization energy (I*) is calculated via $I^* = WF + (E_F^*\text{-}E_V)$. b) top panel: trPL measurements of perovskite on quartz treated with the different molecules. Bottom panel: extracted differential decay times. c) Same measurement on the identical stacks after C_{60} deposition on top. d) and e) trSPV measurements of (un)treated perovskite films on quartz without and with C_{60}. All surface treatments lead to a surface photovoltage even in the absence of the ETL, indicating charge separation induced by an enhanced n-type character on the surface. In the case of stacks with C_{60}, the SPV amplitude is enhanced by the surface treatments (except for TOPO) by enhanced charge carrier separation.

Final State Yield Spectroscopy, CFSYS, measurements depicted in Figure S11b, Supporting Information respectively). On solar cell-like layer stacks, especially with perovskite absorber, it has been observed that the incident photons for photoelectron spectroscopy (PES) measurements can lead to a substantial build-up of surface photovoltage during the measurement.[61] The energetic positions here are corrected by directly observing the Fermi edge in the spectra and considering this–thus, the Fermi level *at the surface*–as the origin of the binding energy axis. The surface dipole, being a shift of the work function (WF) and ionization energy (I*) in equal amounts, is most significant for PTsO with 0.22 eV, followed by PCl with 0.16 eV, PI with 0.14 eV and PTFSI with 0.02 eV. On the other hand, the n-type character, being the relative shift of the work function toward the conduction band with respect to the reference, is largest for PCl, followed by PI, while there are negligible changes for PTFSI and a more p-type surface for PTsO. Overall, this is in line with the QFLS trends, where a higher dipole in combination with a more significant n-type character coincides with a higher implied voltage. The similarity of the TFSI sample to the reference might point to another working mechanism that additionally plays a role, for example with the physical separation of C_{60} and perovskite, resulting in the separation of the wavefunctions and thus a depinning of the Fermi level at the interface, as a possible explanation for the beneficial effects.[9] We excluded the degradation of the surface during the CFSYS measurements by performing several sequential scans and XPS measurements of the Pb4f region after the CFSYS measurements. Furthermore, the degradation due to X-rays was monitored by a second Pb4f measurement at the end of the sequence, showing a slight increase in Pb^0 only for the reference (Figure S9b, Supporting Information). In accordance, as CFSYS can probe the density of occupied states over a very high dynamic range, we also directly assessed the occupied defect states in the bandgap and found that as compared to the reference sample, all surface treatments reduce the occupied states in the bandgap. This reduction indicates chemical passivation of surface defects.

Now, we turn our focus to the carrier dynamics to obtain a better understanding on the correlation of the carrier recombination (from photoluminescence) and energetics (from photoelectron spectroscopy) as already discussed, with carrier extraction observed by transient techniques, specifically, transient photoluminescence (trPL) and transient surface photovoltage (trSPV). Figure 3b,c show trPL measurements (top panel) together with the derived differential lifetimes, for stacks with and without C_{60}, respectively. Without C_{60}, there are only minor differences observable, with a continuously increasing differential lifetime for all sample stacks, reaching several tens of microseconds and the highest values for TOPO passivated samples. An initial short decay time with a fast increase is observed for PCl and PTFSI, indicating a faster separation of charge carriers.[62] Upon adding C_{60} (Figure 3c), the PL signal in all cases shows quenching, with a fast initial decay, followed by a longer one which we associate with carrier separation/extraction and recombination. While the extraction is faster with PTsO than for bare C_{60}, it is slowed down to a small degree for PCl, PI, and more considerably for PTFSI. On the other hand, the fast recombination and decay observed for reference samples is effectively slowed down with the different surface treatments, with a trend following the previously observed QFLS values, that is, (PCl > PI > PTsO > PTFSI). To obtain single-value lifetimes, the differential lifetimes were computed against the QFLS (Figure S12a,b, Supporting Information). Previous reports discussed the difficulty to use averaged lifetimes or such obtained from multiexponential fits for comparing different samples.[63] Instead, the differential lifetimes at the measured steady state QFLS represents the closest approximation to the recombination behavior in a device under V_{OC}.[64] The values obtained for samples previously discussed are summarized in Table S3 (Supporting Information). Samples with C_{60} ETL show a trend in line with the QFLS values, with the highest lifetime obtained for PCl with 8 µs and the lowest for the reference, with 1.75 µs.

In addition, trSPV measurements were conducted on the same samples without and with C_{60}, as presented in (Figure 3d,e) respectively. Our interpretation follows previous works on buried interface modifications.[65] Compared to the non-treated perovskite film, samples with surface treatments and without charge-selective contacts already show an SPV. Thus, as already indicated by trPL measurements, the molecular treatment results in a carrier separation and preferable electron accumulation at the interface (i.e., enhanced n-type character). While initial fast charge build-up is similar for all piperazinium-based surface treatments, a slower build-up (or plateau) following the order PTFSI > PI > PCl is observable, pointing to a charge trapping mechanism or capacitance from ion accumulation on the longer time scales. This is not observable for PTsO-treated samples. Adding C_{60} ETL, the signal is amplified with a trend of PCl ≈ PTsO > PI > PTFSI > Ref, in line with a reduced recombination. The faster rise of the photovoltage when using PTsO fits well to fast extraction indicated also by the initial decay in trPL measurements. Again, a small shoulder at longer times is observable for PI and PCl, while being less pronounced and shifted to earlier times for PTsO. For PTFSI such shoulder is absent, following closely the pristine C_{60} sample track. This secondary rise could indicate a fast extraction into the piperazinium-rich perovskite surface, followed by delayed extraction into the C_{60} ETL. The magnitude of this effect would directly correlate with the amount of piperazinium in the surface layer, being less for PTsO and PTFSI. For the TFSI-treated surface, this effect could be entirely missing due to the additional lower dipole and the mostly negligible impact of the surface treatment in terms of energetics and reduced recombination. Upon switching the substrate to glass/ITO/2PACz, the same trends can be observed (Figure S13, Supporting Information). In summary, the measurements show a qualitative relation of the charge-build-up and extraction (measured under high injection) and the bend bending (measured under equilibrium). The molecular treatments induce an n-type surface layer, resulting in 1) fast charge separation and voltage build-up followed by 2) trapping of the carriers for highly doped surface layers (PCl and PI).

To correlate the structural and electro-optical analysis with device efficiency, we built complete solar cell devices with the stack ITO/2PACz/$Cs_{0.22}FA_{0.78}Pb(I_{0.85}Br_{0.15})_3$ + 5%$MAPbCl_3$/X/C_{60}/SnO_2/Ag (**Figure 4a**). Their trends in PCE and V_{OC} values match well the ones previously shown for respective half-stacks in QFLS measurements. A maximum PCE of 21.5% was obtained for a PCl-treated device in the reverse scan (see Figure S14, Supporting Information for comparison), with a V_{OC} of 1.28 V, FF of 83.1%, and J_{SC} of 20.2 mA cm^{-2} compared to the reference only reaching 17.6% (V_{OC}: 1.18 V, FF: 74.6%, J_{SC}: 20.1 mA cm^{-2}).

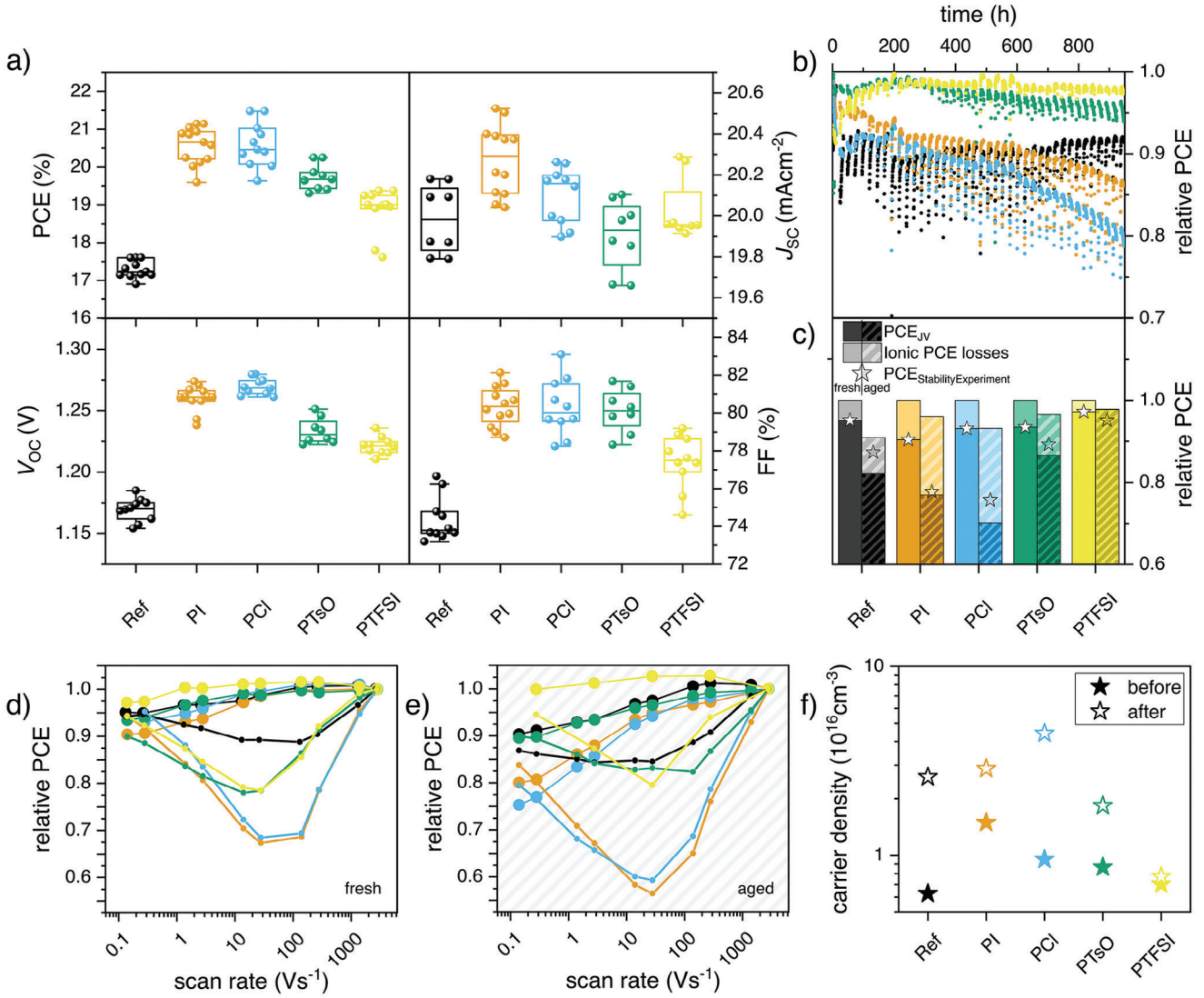

Figure 4. Performance, stability, and ionic losses of solar cell devices. a) Overview of the figure of merit for the different surface treatments compared to the reference device. b) Normalized PCE over 1000h cycled (12h dark, 12h light) illumination ageing at 25 °C in N_2 atmosphere for the cells shown in a). c) Relative PCE of the different devices before and after ageing shows the ion-frozen efficiency measured by fast hysteresis (FH) measurements (d) before and (e) after the ageing experiment. The lightly colored areas in c) show the ionic PCE losses obtained from the difference of steady-state and ion-frozen JV scans in FH measurements, the stars show the efficiencies recorded by conventional JV at the start and end of the cycled MPP ageing experiment. The left and right columns relate to the initial (d) and degraded (e) PCE values before and after the cycled stability experiment respectively. f) Carrier density obtained from dark bias assisted charge extraction (BACE) measurements.

We then measured the stability of these devices under cycled ISOS-LC-1I (ambient, inert), surprisingly showing the opposite trend to the efficiencies, with the lowest degradation losses for PTFSI, followed by PTsO, the reference, PI and PCl (Figure 4b; absolute values Figure S15, Supporting Information, individual tracks Figure S16, Supporting Information). Current–voltage measurements performed at the beginning and end of each light cycle show mainly losses of FF and J_{SC} (Figure S17, Supporting Information), also in line with U_{MPP} and J_{MPP} data (Figure S18, Supporting Information), hinting at an ion-induced loss mechanism.[27] When looking at selected light cycles, a difference in behavior for the devices featuring different treatments, as well as a change over time of this behavior is observable (Figure S19, Supporting Information). Overall, the light cycles can be separated into two phases: i) an initial, short, positive light-soaking phase (i.e., PCE increases), which is sometimes missing, and ii) a second, long phase either showing positive, negative or no light-soaking. The reference sample initially positively light soaks for the whole cycle, while toward the end of the measurement it separates into an elongated light soaking phase and a second phase that changes from a weaker light soaking to a stabilized PCE value toward the end of the measurement. This metastability of continuously increasing light soaking time was reported for measurements under real-world conditions and has been associated with the migration of mobile ions.[25,26] Since the metastability negatively influences the energy yield over time, our results

further emphasize the necessity for cycled light experiments. The treated devices show a strong burn-in in the first 12h under light and a recovery in the dark, following the trends in stability observed over the whole measurement: While the burn-in is similar for PTsO and PTFSI, it is stronger for PI and the strongest for PCl. Also, PTFSI shows a strong recovery in the dark together with a rise in efficiency over the first 100h. PTsO and PI moderately recover, while for PCl almost no recovery is observable. While PTsO always shows a pronounced secondary decay phase, it recovers almost entirely in the dark. The experiment shows, how initial metastability can provide insights into long-term stability and the importance of healing in the dark for perovskite solar cells, being in line with other studies.[25]

To gain more insights into the origin of these losses, we measured fast hysteresis (i.e., *JV* measurements over a wide scan speed range)[27,28] before and after the prolonged ageing to obtain insights on the ionic contribution to the losses, with a summary shown in Figure 4c and the individual fast hysteresis (FH) measurements in Figure 4d,e (absolute values: Figure S21a,b, Supporting Information; relative values Figure S20, Supporting Information). The plot shows the PCE before and after the cycled ageing of nearly 1000h (left (full) and right (striped) bar respectively), with the ionic losses as greyed-out areas. Here, ionic losses refer to the difference of steady-state (slowest scan rate) and ion-frozen (fastest scan rate) PCE values from FH measurements. The largest ionic losses are observed for PCI followed by PI, giving the overall trend Cl^-> I^- > Ref > TsO^- > $TFSI^-$. Notably, these losses are primarily driven by J_{sc} losses as shown in the supporting information, while the FF losses partially transfer into permanent ageing losses (Figure S21a, Supporting Information). For comparison, the efficiencies recorded by conventional *JV* measurements at the start and end of the cycled MPP ageing experiment are shown as stars, which match the FH result reasonably well (while the small uncertainties between the steady-state PCE obtained by conventional *JV* and FH is attributed to the meta-stable behavior of the cells). Respective values of the ion-frozen and steady-state-efficiency were taken from *JV* measurements with the fastest (2800 Vs^{-1}) and slowest (140 mVs^{-1}) scan rates. Only minor changes of the ion-frozen efficiency can be observed during ageing. At the same time, the main contribution to the ageing losses is ionic in nature, mainly impacting FF and J_{SC} (see also *JV*s recorded before and after the ageing in Figure S20, Supporting Information). This is in line with the *JV* measurements recorded during the ageing experiment, with the retrieved parameters of J_{SC}, V_{OC}, FF, and PCE shown in Figure S17 (Supporting Information). Using the ion transit time, previously demonstrated to correspond to the scan time at maximum hysteresis in FH measurements (≈30 Vs^{-1} for all samples), we calculate a diffusion coefficient of 1.51 10^{-9} cm^2 s^{-1} for the mobile ion species in our samples (see Note 1 in the SI). This value aligns well with those reported in the literature for iodide ions in metal halide perovskite films.[66] Additional bias-assisted charge extraction (BACE) measurements (Figure S21c, Supporting Information) show the highest increase in mobile ion density after the ageing by a factor of 5 for PCl. We note the trends observed in the ion density obtained from BACE after ageing (Device PCl > PI > Ref > PTsO > PTFSI) match the stability trends observed as well as the fast-hysteresis measurements, yet alone they are not sufficient to explain the observed trends fully. Previous works showed that ion densities tend to have a negative influence when changing over orders of magnitude, whereas in the conducted measurements, they remain within the range of 10^{16} cm^{-3}. We note that BACE was measured after keeping the device in the dark for a short time after the MPP measurements. This will displace the ions to the contacts by the built-in field, or lead to recovery (reduction) of the ion density.[28] Hence, we consider the ion densities obtained after ageing as a lower limit of the ion density that is present under illumination. Overall, we see that except for PTSO and PTFSI the ionic losses are magnified by the surface treatments.

We attribute the ionic losses to field screening caused by the movement of mobile ions to the transport layers, as previously discussed in more detail, which effectively reduces the FF and J_{SC} by lowering the driving force for drift and extraction. While diffusion lengths and lifetimes are long in perovskite absorbers, the employed undoped transport layers necessitate to have a field (throughout the bulk) for effective extraction.[67] Moreover, the absence of a field would lead to reverse fields in forward bias which greatly amplifies interfacial and other non-radiative recombination losses.

We speculate that the increase in ionic losses observed for several passivation layers (PI, PCI) may be attributed to the following mechanism: A thin perovskite surface layer of enhanced n-type character leads to the formation of an electron accumulation layer. Photogenerated electrons are thus driven toward this accumulation layer, and then extracted efficiently to the C_{60} layer. This is in line with the trSPV measurements conducted. The driving force for extraction to achieve maximum FF and J_{SC} values is the gradient of the electron Quasi–Fermi level (Δ_{eQFLS}). Given (1) Δ_{eQFLS} between perovskite and C_{60} decreases in dependence of the n-type character enhancement and (2) increasing field redistribution by the growing mobile ion densities, the extraction will be influenced negatively more quickly with increasing n-type character on the surface (smaller Δ_{eQFLS}).

To test these assumptions, we conducted drift-diffusion simulations incorporating mobile ions using the software SETFOS from FLUXIM.[68] Following previous research, we assumed an increase in ion density with ageing, contributing to elevated ionic losses.[28] The parameters used for the calculations are summarized in Table S4 (Supporting Information). In our model, we parameterize the accumulation layer by a 2 nm thin perovskite layer with varying doping densities n_{surf} to reflect the variations in band bending observed in photoelectron spectroscopy measurements. While a true ionisation process, as known from inorganic semiconductors, is unlikely, this approach accounts for additional positive fix charges and increased electron density. We justify this by assuming that the cation and anion of the salt are incorporated into the A and X sites of the ABX_3 perovskite crystal structure, respectively. With the cation electrostatically bound via the ammonium moiety at the A site position, the opposite amine group, possessing a free electron pair, can contribute to the conduction band's electron density. This can occur either through a ligand-like bonding to lead, hydrogen bonding to other A-site cations, or partial ionization, which leaves the amine electron-deficient while increasing the electron density in the conduction band.

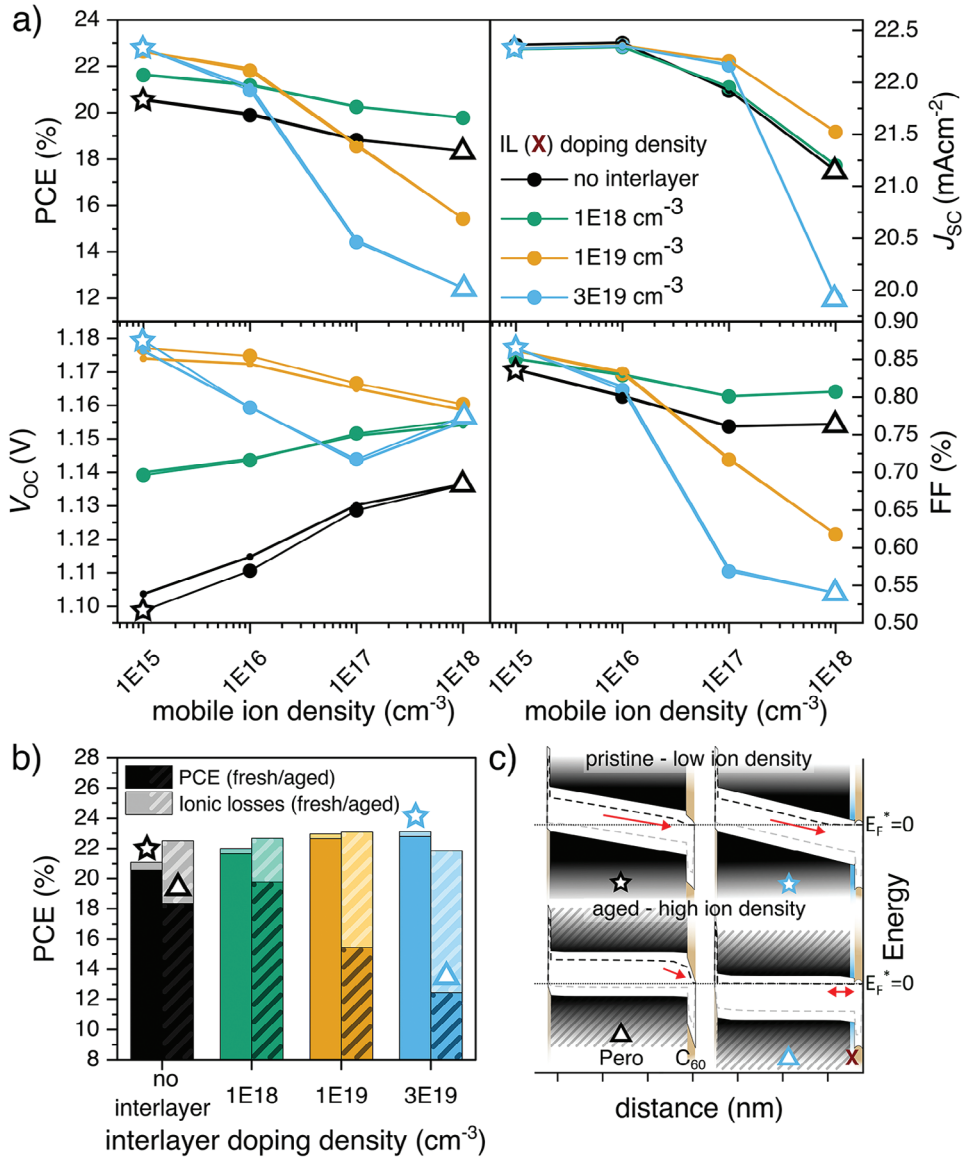

Figure 5. Numerical simulation of solar cell devices with different n-type surfaces. Overview of simulated performance parameters against increasing mobile ion defect densities in solar cell stacks of ITO/2PACz/Perovskite (1.63 eV)/X/C_{60}/BCP/Ag obtained from numerical simulation. X refers to a 2 nm interlayers with different degrees of n-type doping density (legend). b) Absolute PCE of these devices before (left) and after (right) ageing (i.e. using lowest and highest mobile ion densities of 10^{15} and 10^{18} cm^{-3} respectively): The more lightly colored parts of the bars show the ionic PCE losses obtained from the difference between steady-state and ion-frozen JV scans in FH measurements. c) Simulated band diagrams at J_{SC} using mobile ion densities of 10^{15} (pristine) and 10^{18} cm^{-3} (aged) for reference devices and such with n-doped interlayer "X" using a doping density of 3x10^{9} cm^{-3}. Devices with an n-doped interlayer "X" show reduced extraction due to reduced electric fields.

The simulated Fast-Hysteresis measurements are presented in Figures S24–S27 (Supporting Information), with a summary of steady-state (i.e., low scan speeds) performance metrics shown in **Figure** 5a (see Figure S28, Supporting Information for normalized data). An increase in simulated absolute efficiency was observed in pristine devices with low ion densities, with saturation occurring at ≈10^{-19} cm^{-3}, primarily due to enhanced V_{OC} and Fill Factor. In agreement with our experimental observations, higher bend bending, achieved with doping levels above 10^{-18} cm^{-3}, leads to a more pronounced decline in performance as ion density increases. Figure 5b summarizes the comparison between pristine and aged devices across different simulated doping densities of the interlayer (see Figure S29, Supporting Information for normalized data), which aligns well with the data previously discussed for the different treatments (Figure 4c–f). Comparing the simulated band diagrams at J_{SC} for pristine and aged devices with no interlayer and X interlayer with doping density of 10^{-19} cm^{-3} (Figure 5c), the latter shows a stronger field redistribution and thus lower driving force for extraction with increased ion densities. Figure S30 (Supporting Information) gives an overview of the simulated band diagrams for different conditions. We consider the amplification of ionic losses due to

surface treatments a plausible explanation for the observed trends, though other mechanisms, such as surface reactions, cannot be entirely ruled out.

Previous results demonstrated improved stability upon introducing related surface treatments based on diamines.[18,69] The discrepancy to our results could be attributed to: 1) the use of lower salt concentrations, likely due to better initial energy alignment (e.g., for narrower bandgap absorbers), 2) potentially by accepting a trade-off in V_{OC} or 3) by a higher stability against ionic losses.

3. Conclusion

We have investigated the impact of the anion type in piperazinium salt surface treatments on the efficiency and stability of 1.68 eV perovskite solar cells.

We find a strong correlation between surface band bending, the surface dipole of the treated perovskite films (obtained via photoemission spectroscopy), and the open-circuit voltage of the final device, which correlates with data from transient surface photovoltage (trSPV), transient photoluminescence (trPL), and photoluminescence quantum yield (PLQY) measurements. Chloride-based treatments achieve the highest power conversion efficiencies of 21.5% with voltages up to 1.28V, which correlate with the most substantial band bending at the interface with C_{60}. Contrary to other reports, our findings indicate that higher PCE does not necessarily correlate with increased stability. Fast-Hysteresis measurements show that the redistribution of the electric field by ion accumulation causes extraction losses, which reduces J_{SC} and FF and has a significant impact on the operational stability of the devices. In this regard, we find that small halide anions, such as iodide and chloride, result in higher voltages and efficiencies due to enhanced electron accumulation at the perovskite/C_{60} interface; however, these devices exhibit faster degradation. Piperazinium tosylate (PTsO) and piperazinium bistriflimide (PTFSI) on the other hand have a more negligible impact on perovskite surface energetics and carrier dynamics, however, do not achieve comparable voltages. Yet, they offer potentially the best trade-off between efficiency and stability. We speculate that the observed trends are a result of an additional surface-junction between perovskite and fullerene C_{60}, slowing down electron extraction faster with increasing ion densities. This was further verified by numerical simulation, showing that ionic losses are magnified for perovskite surfaces with strong n-type character.

Mitigating ion-induced losses through strategies such as increasing the activation energy for ion migration via bulk modifications, accelerating self-healing in the dark, or designing more resilient interfaces and contact materials, needs further attention in the future.

4. Experimental Section

Materials: Indium-tin-oxide (ITO) coated glass substrates (15 Ohm sq^{-1}) were purchased from Automated Research GmbH. Dimethyl sulfoxide (DMSO, ≥99.9%), dimethylformamide (DMF, 99.8%), Anisole (99.7%), and Isopropanol (IPA, 99.5%) were purchased from Sigma Aldrich. Formamidinium iodide (FAI, 99.99%) and methylammonium chloride (MACl, 99.99%) were purchased from Dyenamo. PbI_2 (99.99%), $PbBr_2$ (≥98.0%), $PbCl_2$ (>99.0%), and [2-(9H-Carbazol-9-yl)ethyl]phosphonic Acid (2PACz), >98.0%) were purchased from TCI. CsI (99.999%) was purchased from abcr GmbH. Ethanol (EtOH, anhydrous) was obtained from VWR. C60 (sublimed; 99.95%) was obtained from CreaPhys GmbH. The ceramic 4-inch IZO target (In_2O_3 with 10%wt. ZnO) was purchased from robeko GmbH & Co. KG. TDMASn (tetrakis(dimethylamino)tin(IV), 99% (99.99%-Sn)) was purchased from STREM CHEMICALS, INC. All the materials were used as received without any purification.

Piperazinium iodide (PI), piperazinium chloride (PCl), piperazinium tosylate (PTsO), and piperazinium bistriflimide (PTFSI) were synthesized by Dr. Mantione at POLYMAT according to literature.[59,70] Briefly, for PI, PCl, and PTsO: piperazine (1 eq) was dissolved in ethanol (15 ml g^{-1}) and placed in an ice-water bath. The conjugated acid HX (2 eq) was diluted and added dropwise under rigorous stirring. After 30 min of additional stirring, the solvent was evaporated, and the resulting solid, was filtered and washed with ethyl acetate several times before being dried under vacuum. For PTFSI: PI has been dissolved in water (5 mL g^{-1}) and 2 eq of LiTFSI has been added in one shot, using a water solution 2 M. The resulting solid has been filtered, washed with water and dried.1H and 19F NMR were according to the literature.

Triple Halide Perovskite (3Hal) Solution: First, 1.4M "FACs" perovskite ($Cs_{0.22}FA_{0.78}Pb(I_{0.85}Br_{0.15})_3$) solution in 3:1 DMF:DMSO was shaken at room temperature (RT) overnight. 1h prior the layer deposition, the whole solution was transferred to a vial containing 5mol% of $MAPbCl_3$ and then shaken 10min at 60 °C followed by 50 min at RT. Directly before use, the solution was filtered using a 0.22µm polytetrafluoroethylene membrane. Exemplary amounts of chemicals for 1 ml of 1.4 M solution are: 500 mg PbI_2, 116 mg $PbBr_2$, 188 mg FAI, 80 mg CsI (weighed into one vial) + 4.7 mg MACl, 19.5 mg $PbCl_2$ (in another vial).

The triple halide perovskite was adapted due to its phase stability, better film quality, and higher voltage potential (comparing PLQY of the film on quartz to commonly employed triple cation (3Cat) or FACs perovskites).[11,47]

Single Junction Solar Cell Fabrication: The solar cell configuration is ITO/2PACz/3Hal/(PX) /C_{60}(16nm)/SnO_2(15nm)/Ag(100nm). Glass/ITO substrates were cleaned by ultra-sonication in detergent (Hellmanex, 2% in DI-water), water, acetone, and IPA for 15 min each. Dried substrates were then treated by UV/Ozone for 15 min before being transferred into the nitrogen glovebox. All following processing steps were conducted in inert atmosphere with oxygen and water levels maintained below 0.5 ppm.

For the HTL, 3mM 2PACz solution (≈1 mg mL^{-1} in ethanol) was spin-coated at 3000 rpm for 30 sec and annealed at 100 °C for 10 min. Thereafter, 70µL of perovskite solution was spread on the substrate and spin-coated at 3500 rpm for 40 s with an acceleration of 700 rpm s^{-1}. 300µL of anisole was applied as the antisolvent 25s after the start of the process. The film was then annealed for 20min at 100 °C.

For the molecular surface treatment using PX salts, a 1.4 mM solution of the respective salt (PI: 0.3 mg mL^{-1}, PCl: 0.172 mg mL^{-1}, PTsO: 0.362 mg mL^{-1}, PTFSI: 0.515 mg mL^{-1}) in IPA was dynamically spin-coated at 5000 rpm for 20 s. The films were annealed for 2min at 100 °C, followed by, repeating the same spin-coating and annealing procedure with pure IPA to remove excess powder.

Substrates were transferred to the evaporation system and 16nm C_{60} were subsequently deposited by thermal evaporation using an increasing rate of 0.01–0.16 As^{-1}. After finishing the C_{60} deposition, the substrates were transferred to the atomic layer deposition (ALD) system (Ardradiance GEMStar) to deposit 15nm of SnO2 at 80 °C using the precursor tetrakis(dimethylamino)tin(IV) and deionized water as oxidant. Finally, the 100nm Ag electrode was evaporated at an increasing rate of 0.1–1As^{-1} by thermal evaporation using a shadow mask. The active area was defined to 0.16cm^2.

Absolute Photoluminescence (PL): Absolute photoluminescence was measured with a prototype of the "LuQY Pro" setup by QYB. The PL signal was collected with a fiber connected to a CCD-array spectrometer (Ocean Optics). Samples were excited with a continuous-wave laser by Insaneware at 532 nm emission wavelength, a photon flux of ≈1.2E16 photons s^{-1}, and a spot size on the sample of 0.12 cm^2 (≈1-sun-equivalent excitation

fluence, calibrated with a certified silicon reference cell). The Quasi–Fermi level splitting (QLFS)was then calculated via:

$$QFLS_{PL} = k_B T \cdot \ln\left(PLQY \cdot \frac{J_G}{J_{0,rad}}\right) \quad (1)$$

with $J_{0,rad}$ being the radiative thermal recombination current density in the dark, k_B the Boltzmann constant, T the temperature and J_G the generation current density. The generation current density J_G was approximated with the short-circuit current density of the complete solar cell device (≈20mAcm^{-2}). Similarly, $J_{0,rad}$ was calculated by integrating the overlap of the external quantum efficiency of the device (EQE) with the black body spectrum ϕ_{BB} at 300 K over the energy.

$$J_{0,rad} = \int EQE \cdot \phi_{BB} dE \quad (2)$$

with

$$\phi_{BB} = \frac{1}{4^2 \hbar^3 c^2} \cdot \frac{E^2}{\exp\left(\frac{E}{k_B T}\right) - 1} \quad (3)$$

This resulted in a $J_{0,rad}$ value of 9.8×10^{-22} A m^{-2}.

Transient Photoluminescence (trPL): Measurements were performed with a home-built confocal PL setup in air on epoxy/glass encapsulated samples. The setup featured a "80:20"- "transmission:reflection"-beam splitter to separate the excitation and detection paths. A 700 nm diode laser (IB-705-B laser head with Taiko driver, Picoquant) with a pulse duration of ≈100 ps and a repetition rate of 10 kHz was used for excitation from the substrate side. The laser beam was passed through a cleanup filter (FF01-700/13–25, Semrock) and the energy of the laser beam was tuned by a linear-gradient neutral density filter to ≈0.2µW (≈0.8µW readout on powermeter).

An off-axis parabolic mirror with 5 cm focal length has been used for the focus and PL collection. The laser spot size is a circle with ≈250 µm diameter. A silicon single-photon avalanche diode (Laser Components COUNT-50) has been employed for the PL detection, and the signal was cut by a 715nm long-pass filter (FF01-715/LP-25, Semrock). The PL count and decay histogram were recorded by a TimeHarp260 Nano time-correlated single photon counting module (Picoquant).

The decay curve was fitted by an arbitrary sum of instantaneous exponential slopes (usually 3–5) to compute the differential lifetime.

$$\tau = -\left\{ d \ln\left(\frac{\phi(t)}{dt}\right)\right\}^{-1} \quad (4)$$

where $\phi(t)$ is the time-dependent photon flux. This representation allows to access the "lifetime" at each point of time.[63,71] To obtain single lifetime values, it was assumed that at t = 0 the carrier concentration was the same in all samples, depending on the absorption coefficient at the laser wavelength (α(700 nm) = 4.5E5 cm^{-1}), the thickness of the sample (d = 450 nm), the power and repetition rate of the laser (P = 0.802 µW, k = 10 000 Hz), the laser spot size and the bandgap. The carrier concentration was further used to calculate the QFLS.[64]

Transient Photovoltage (trSPV): Measurements were performed on a home-built setup in the air on epoxy/glass encapsulated samples. The samples were excited from the substrate side by 563 nm laser light from a diode pumped pulse laser (Nd:YAG, EKSPLA, NT230-50, duration time of laser pulses ≈3ns) with a spectral cleaning unit. The laser intensity was set to ≈0.1-sun-equivalent excitation fluence by a set of neutral density filters. The SPV transients were measured at a sampling frequency of 2 Hz averaging over 20 measurements using an oscilloscope card (Gage, CSE 1622- 4GS, 200 MS s^{-1}) together with an in-house developed software for logarithmic read-out.[72]

Transient Absorption (TA): A Ti:Sapphire amplifier system (Coherent Libra) operating at 1 kHz generated ≈46fs pulses and an Opera Solo OPO was used to generate the white light probe beam and the pump beam pulses respectively. The pump pulses were chopped with a mechanical chopper at 500 Hz. Generation of the broad band white light probe beam was done in a home-built noncollinear optical parametric amplifier with a 3mm thick YAG crystal. The probe pulse was delayed with a 1.5 m long home built mechanical delay stage with a moving retro reflector and then split into a reference beam and the actual probe beam through the sample. Pump and probe overlap was optimized at the position of the sample. The transmitted probe light was detected with an home built ultrafast prism spectrometer and the dispersed light was collected with a VIS CMOS dual-line array detector driven and read out by a custom-built board from Entwicklungsbüro Stresing. For all measurements, the pump intensity was fixed to 8 µJ cm^{-2} at 400nm.

Current–Voltage Curves (JV): Measurements were recorded inside a nitrogen-filled glovebox. Prior the measurements, the solar simulator (Oriel LCS-100) intensity was calibrated to AM1.5G 1-sun-equivalent with a filtered KG3 Silicon reference solar cell. The scans were performed with a Keithley 2400 source-measure unit controlled via a custom LabView program. The individual contacts were measured by a 2-point-probe method and the following parameters were used: voltage range −0.01–1.30V, step size 0.02V, integration and settling time 20ms. The boxes in the PV parameter boxplots indicate the 25/75 percentiles and the line indicates respective mean values.

External Quantum Efficiency (EQE): Spectra were measured using an Oriel Instruments QEPVSI-b system equipped with a Newport 300 W xenon arc lamp, all controlled by TracQ-Basic software. Prior to each measurement, the system was calibrated using a silicon reference cell with a known spectral response. The electrical response of the test device was recorded using a Stanford Research SR830 Lock-In amplifier, with a time constant of 0.3 s, and analyzed in TracQ. Typically, the short-circuit current mismatch between the integrated external quantum efficiency (EQE) multiplied by AM1.5G irradiance and the values obtained from J–V scans was ≈1%, assuming accurate knowledge of the cell area and accounting for shadowing effects during metal evaporation.

Fourier Transform Photocurrent Spectroscopy (FTPS): Spectra were measured in the air using the Enlitech PECT-600 system with encapsulated samples. Calibration was performed beforehand using a silicon cell with a known spectral response. Measurements were taken with a step size of 5 nm.

Time-of-Flight Secondary-Ion-Mass-Spectrometry (ToF-SIMS): Depth profiles were measured with an ion-ToF ToF-SIMS Spectrometer following previously developed protocols.[73] The setup featured a 30keV BiMn primary ion gun for analysis. A primary ion beam of 30KeV Bi_3^+ (0.8pA pulsed beam current) was employed for high mass resolution depth profiles of 50 × 50µm size analyzed with a 128:128 primary beam raster. For sputter depth profiling a 600eV Cs^+ ion beam (2.6nA sputter current) with a raster of 150 × 150µm was used.

X-Ray Diffraction (XRD): Patterns were obtained using a Bruker D8 diffractometer configured in Bragg–Brentano geometry. All measurements employed Cu K-alpha radiation generated by an X-ray tube operating at 40 mA and 40 kV. Data were collected with a step size of 0.02° 2θ and an integration time of 0.8 s.

Grazing-Incidence Wide-Angle X-Ray Scattering (GIWAXS): Measurements were performed at mySpot beamline, BESSY II.[74] The samples were measured in reflection mode with incidence angles from 0.1 to 2° (39 scans, 0.05° interval), using radiation energy of 9 keV (λ = 1.378 Å). The size of the beam was ≈100µm. The 2D images were plotted and integrated using Dpdak and GIXSGUI software.[75]

Scanning Electron Microscopy (SEM): Micrographs were recorded with a Zeiss Merlin Gemini 2 microscope using an acceleration voltage of 3 kV.

Photoelectron Spectroscopy (PES) Measurements with Near UV Excitation: Measurements were conducted in UHV with a base pressure of <10^{-9} mbar. Samples were transferred in an N_2-filled unit, avoiding air exposure, and contacted via metal fingers on the conductive ITO substrate. A xenon XBO lamp with a double grating monochromator provided a photon flux >10^{11} s^{-1}cm^{-2} up to a photon energy of ≈7 eV. The actual photon flux was monitored by a calibrated photodiode, allowing for

the determination of photoelectron yield. Photoelectrons were collected in a hemispheric electron analyzer EA10P (SPECS) with energy resolutions of 125 and 250 meV.Two near-UV PES variants were used: i) UPS with fixed excitation (6.5 eV), ii) Photoelectron yield measurements in constant final state mode (CFSYS) with varying photon energy (3.7 – 7.3 eV). The work function was determined by fitting a Boltzmann function to the secondary electron cut-off in the near-UV UPS spectra. The CFSYS spectra enable to determine the density of occupied states up to the Fermi edge E_F^*. Due to surface photovoltage, induced by the measurement illumination itself, the surface Fermi level E_F^* might shift with respect to the contacted Fermi level of the ITO substrate.[61] With a very high S/N ratio and the direct observation of the Fermi edge in the spectra, it was corrected for this and the energetic positions relative to the actual Fermi level at the sample front surface are provided. The valence band maxima were determined using a previously presented model including a parabolic band edge and an exponential band tail.[11,61] The conduction band energies were calculated by adding the bandgap energy (determined from EQE) to the obtained valence band energy levels. Given the differences in the chemical composition of the surface, which might have resulted in a bandgap widening, the CBM values were more qualitative than quantitative.

X-Ray Photoelectron Spectroscopy (XPS): Measurements were performed with Al-Kα excitation (1486.6 eV, 14kV, 300W) in a different UHV System (base presser $<10^{-10}$ mbar, with equally fully inert sample transfer to protect the sample surface from contaminations. A hemispheric PHOIBOS 150 1D-DLD analyzer (SPECS) was used in medium area lens mode with a pass energy of 30eV and averaging over several scans for each core level. For all samples, the same measurement protocol was applied with an initial and final detailed measurement of the Pb4f and N1s core level. A minor shift of <0.1eV toward lower binding energies was observed for the Pb4f peak position. A formation of Pb^0 was mostly not observed, besides the reference sample with a small shoulder in the Pb4f core level appearing toward lower binding energy.

Long-Term Stability: Measurements were recorded with a custom-built high-throughput ageing setup following previous protocols.[76] A perturb-and-observe-algorithm[77] with a delay time of 1s and a voltage step-width of 0.01V was applied to each cell individually and the MPP merits updated every 2min. 1-sun-equivalent illumination was provided by a metal-halide lamp using a H6 filter,[11] with the intensity actively controlled with an irradiation-sensor calibrated with a KG3-filtered silicon reference cell. The device temperature was maintained by actively controlled Peltier-elements using heat pads for direct thermal coupling.

The light-cycling experiment according to ISOS-LC-1I (12 h/12h light/dark, N_2 atmosphere, 25 °C) used a shutter system for fully shading the cells while simultaneously disconnecting the MPP-trackers. Additionally, JV measurements were done at the beginning and end of each cycle.

Fast-Hysteresis (FH): Measurement curves were obtained using a triangular voltage pulse starting from open-circuit (V_{OC}), followed by a reverse sweep to −0.1 V and a forward sweep back to V_{OC}, with variable scan speeds (V s^{-1}) using a FastChar UG system. The hold time at VOC was five times longer than the total scan time. The voltage response was measured with an oscilloscope and an external load resistance of ≤10 Ω, using a function generator and a home-built power amplifier (4×). Testing conditions matched those of standard J–V measurements.

Bias Assisted Charge Extraction (BACE): Measurements were performed by recording the current transients with a Keithley 2400 source meter, controlled by a custom LabView program. The device was initially held at a voltage near open-circuit voltage (VOC) to balance the injected charge with the short-circuit current. After a preset delay, a bias of 0 V was applied to extract the injected and capacitive charge. The delay times were ≈5x longer than the extraction time (≈5–10 s) to allow ionic charges to distribute in the active layer. The extracted charge was obtained by integrating the current transient.

Numerical Simulation: The simulations were performed using SETFOS.[68] The program numerically solves a system of three coupled equations, namely the Poisson equation, the continuity equation, and the drift–diffusion equation.[78]

Supporting Information

Supporting Information is available from the Wiley Online Library or from the author.

Acknowledgements

The authors thank J.B., M.C., C.F., M.W., T.L., and H.H. for the technical support in HySPRINT Helmholtz Innovation Lab; A. Miaskiewic for SEM technical support; The authors thank T.D. for fruitful discussions and providing the HZB SPV laboratory facilities. The authors thank the Helmholtz Association for funding the project TAPAS (Tandem Perovskite and Silicon solar cells—Advanced optoelectrical characterization, modeling, and stability) within the EU partnering program. D.M. thanks grant RYC2021-031668-I funded by MCIU/AEI /10.13039/501100011033 and by the European Union NextGenerationEU/PRTR. M.T. and F.S. thank the Slovenian Research and Innovation Agency (ARIS), program P2-0415. This work was authored in part by the National Renewable Energy Laboratory, operated by Alliance for Sustainable Energy, LLC, for the U.S. Department of Energy (DOE) under Contract No. DE-AC36-08GO28308. The NREL authors acknowledge research support from the HydroGEN Advanced Water Splitting Materials Consortium, established as part of the Energy Materials Network under the U.S. Department of Energy, Office of Energy Efficiency and Renewable Energy, Hydrogen and Fuel Cell Technologies Office. The views expressed in the article do not necessarily represent the views of the DOE or the U.S. Government. The U.S. Government retains and the publisher, by accepting the article for publication, acknowledges that the U.S. Government retains a nonexclusive, paid-up, irrevocable, worldwide license to publish or reproduce the published form of this work, or allow others to do so, for U.S. Government purposes.

Open access funding enabled and organized by Projekt DEAL.

Conflict of Interest

The authors declare no conflict of interest.

Data Availability Statement

The data that support the findings of this study are available from the corresponding author upon reasonable request.

Keywords

interface passivation, ionic losses, perovskite solar cells, stability

Received: October 11, 2024
Revised: November 27, 2024
Published online: December 17, 2024

[1] "Best Research-Cell Efficiency Chart," can be found under, https://www.nrel.gov/pv/cell-efficiency.html, (accessed: September 2024).
[2] S. Liu, J. Li, W. Xiao, R. Chen, Z. Sun, Y. Zhang, X. Lei, S. Hu, M. Kober-Czerny, J. Wang, F. Ren, Q. Zhou, H. Raza, Y. Gao, Y. Ji, S. Li, H. Li, L. Qiu, W. Huang, Y. Zhao, B. Xu, Z. Liu, H. J. Snaith, N.-G. Park, W. Chen, *Nature* **2024**, *632*, 536.
[3] M. A. Green, E. D. Dunlop, M. Yoshita, N. Kopidakis, K. Bothe, G. Siefer, D. Hinken, M. Rauer, J. Hohl-Ebinger, X. Hao, *Prog. Photovoltaics* **2024**, *32*, 425.
[4] T. Leijtens, K. A. Bush, R. Prasanna, M. D. McGehee, *Nat. Energy* **2018**, *3*, 828.

[5] Q. Jiang, K. Zhu, *Nat. Rev. Mater.* **2024**, *9*, 399.
[6] D. Menzel, A. Al-Ashouri, A. Tejada, I. Levine, J. A. Guerra, B. Rech, S. Albrecht, L. Korte, *Adv. Energy Mater.* **2022**, *12*, 2201109.
[7] J. Warby, F. Zu, S. Zeiske, E. Gutierrez-Partida, L. Frohloff, S. Kahmann, K. Frohna, E. Mosconi, E. Radicchi, F. Lang, S. Shah, F. Peña-Camargo, H. Hempel, T. Unold, N. Koch, N. Koch, A. Armin, F. De Angelis, S. D. Stranks, D. Neher, M. Stolterfoht, *Adv. Energy Mater.* **2022**, *12*, 2103567.
[8] R. R. Pradhan, M. K. Eswaran, A. S. Subbiah, A. Babayigit, S. De Wolf, U. Schwingenschlögl, *ACS Appl. Energy Mater.* **2023**, *6*, 4111.
[9] J. Liu, M. De Bastiani, E. Aydin, G. T. Harrison, Y. Gao, R. R. Pradhan, M. K. Eswaran, M. Mandal, W. Yan, A. Seitkhan, M. Babics, A. S. Subbiah, E. Ugur, F. Xu, L. Xu, M. Wang, A. ur Rehman, A. Razzaq, J. Kang, R. Azmi, A. A. Said, F. H. Isikgor, T. G. Allen, D. Andrienko, U. Schwingenschlögl, F. Laquai, S. De Wolf, *Science* **2022**, *302*, eabn8910.
[10] W. Xu, L. J. F. Hart, B. Moss, P. Caprioglio, T. J. Macdonald, F. Furlan, J. Panidi, R. D. J. Oliver, R. A. Pacalaj, M. Heeney, N. Gasparini, H. J. Snaith, P. R. F. Barnes, J. R. Durrant, *Adv. Energy Mater.* **2023**, *13*, 2301102.
[11] S. Mariotti, E. Köhnen, F. Scheler, K. Sveinbjörnsson, L. Zimmermann, M. Piot, F. Yang, B. Li, J. Warby, A. Musiienko, D. Menzel, F. Lang, S. Keßler, I. Levine, D. Mantione, A. Al-Ashouri, M. S. Härtel, K. Xu, A. Cruz, J. Kurpiers, P. Wagner, H. Köbler, J. Li, A. Magomedov, D. Mecerreyes, E. Unger, A. Abate, M. Stolterfoht, B. Stannowski, R. Schlatmann, et al., *Science* **2023**, *381*, 63.
[12] H. Min, M. Kim, S.-U. Lee, H. Kim, G. Kim, K. Choi, J. H. Lee, S. I. Seok, *Science* **2019**, *366*, 749.
[13] R. D. J. Oliver, P. Caprioglio, F. Peña-Camargo, L. R. V. Buizza, F. Zu, A. J. Ramadan, S. G. Motti, S. Mahesh, M. M. McCarthy, J. H. Warby, Y.-H. Lin, N. Koch, S. Albrecht, L. M. Herz, M. B. Johnston, D. Neher, M. Stolterfoht, H. J. Snaith, *Energy Environ. Sci.* **2022**, *15*, 714.
[14] P. Caprioglio, J. A. Smith, R. D. J. Oliver, A. Dasgupta, S. Choudhary, M. D. Farrar, A. J. Ramadan, Y.-H. Lin, M. G. Christoforo, J. M. Ball, J. Diekmann, J. Thiesbrummel, K.-A. Zaininger, X. Shen, M. B. Johnston, D. Neher, M. Stolterfoht, H. J. Snaith, *Nat. Commun.* **2023**, *14*, 932.
[15] Z. Wu, E. Bi, L. K. Ono, D. Li, O. M. Bakr, Y. Yan, Y. Qi, *Nano Energy* **2023**, *115*, 108731.
[16] H. Chen, C. Liu, J. Xu, A. Maxwell, W. Zhou, Y. Yang, Q. Zhou, A. S. R. Bati, H. Wan, Z. Wang, L. Zeng, J. Wang, P. Serles, Y. Liu, S. Teale, Y. Liu, M. I. Saidaminov, M. Li, N. Rolston, S. Hoogland, T. Filleter, M. G. Kanatzidis, B. Chen, Z. Ning, E. H. Sargent, *Science* **2024**, *384*, 189.
[17] J. Liu, Y. He, L. Ding, H. Zhang, Q. Li, L. Jia, J. Yu, T. W. Lau, M. Li, Y. Qin, X. Gu, F. Zhang, Q. Li, Y. Yang, S. Zhao, X. Wu, J. Liu, T. Liu, Y. Gao, Y. Wang, X. Dong, H. Chen, P. Li, T. Zhou, M. Yang, X. Ru, F. Peng, S. Yin, M. Qu, D. Zhao, et al., *Nature* **2024**, *635*, 596.
[18] H. Chen, A. Maxwell, C. Li, S. Teale, B. Chen, T. Zhu, E. Ugur, G. Harrison, L. Grater, J. Wang, Z. Wang, L. Zeng, S. M. Park, L. Chen, P. Serles, R. A. Awni, B. Subedi, X. Zheng, C. Xiao, N. J. Podraza, T. Filleter, C. Liu, Y. Yang, J. M. Luther, S. De Wolf, M. G. Kanatzidis, Y. Yan, E. H. Sargent, *Nature* **2023**, *613*, 676.
[19] K. Frohna, C. Chosy, A. Al-Ashouri, F. Scheler, Y.-H. Chiang, M. Dubajic, J. E. Parker, J. M. Walker, L. Zimmermann, T. A. Selby, Y. Lu, B. Roose, S. Albrecht, M. Anaya, S. D. Stranks, *Nature Energy* **2024**, https://doi.org/10.1038/s41560-024-01660-1.
[20] N. T. P. Hartono, H. Köbler, P. Graniero, M. Khenkin, R. Schlatmann, C. Ulbrich, A. Abate, *Nat. Commun.* **2023**, *14*, 4869.
[21] E. Aydin, T. G. Allen, M. De Bastiani, A. Razzaq, L. Xu, E. Ugur, J. Liu, S. De Wolf, *Science* **2024**, *383*, eadh3849.
[22] H. Zhu, S. Teale, M. N. Lintangpradipto, S. Mahesh, B. Chen, M. D. McGehee, E. H. Sargent, O. M. Bakr, *Nat. Rev. Mater.* **2023**, *8*, 569.
[23] M. V. Khenkin, E. A. Katz, A. Abate, G. Bardizza, J. J. Berry, C. Brabec, F. Brunetti, V. Bulović, Q. Burlingame, A. Di Carlo, R. Cheacharoen, Y.-B. Cheng, A. Colsmann, S. Cros, K. Domanski, M. Dusza, C. J. Fell, S. R. Forrest, Y. Galagan, D. Di Girolamo, M. Grätzel, A. Hagfeldt, E. von Hauff, H. Hoppe, J. Kettle, H. Köbler, M. S. Leite, S. Liu, Y.-L. Loo, J. M. Luther, et al., *Nat. Energy* **2020**, *5*, 35.
[24] Y.-T. Huang, S. R. Kavanagh, D. O. Scanlon, A. Walsh, R. L. Z. Hoye, *Nanotechnology* **2021**, *32*, 132004.
[25] M. Khenkin, H. Köbler, M. Remec, R. Roy, U. Erdil, J. Li, N. Phung, G. Adwan, G. Paramasivam, Q. Emery, E. Unger, R. Schlatmann, C. Ulbrich, A. Abate, *Energy Environ. Sci.* **2024**, *17*, 602.
[26] M. Remec, Š. Tomšič, M. Khenkin, Q. Emery, J. Li, F. Scheler, B. Glažar, M. Jankovec, M. Jošt, E. Unger, S. Albrecht, R. Schlatmann, B. Lipovšek, C. Ulbrich, M. Topič, *Adv. Energy Mater.* **2024**, *14*, 2304452.
[27] V. M. Le Corre, J. Diekmann, F. Peña-Camargo, J. Thiesbrummel, N. Tokmoldin, E. Gutierrez-Partida, K. P. Peters, L. Perdigón-Toro, M. H. Futscher, F. Lang, J. Warby, H. J. Snaith, D. Neher, M. Stolterfoht, *Sol. RRL* **2022**, *6*, 2100772.
[28] J. Thiesbrummel, S. Shah, E. Gutierrez-Partida, F. Zu, F. Peña-Camargo, S. Zeiske, J. Diekmann, F. Ye, K. P. Peters, K. O. Brinkmann, P. Caprioglio, A. Dasgupta, S. Seo, F. A. Adeleye, J. Warby, Q. Jeangros, F. Lang, S. Zhang, S. Albrecht, T. Riedl, A. Armin, D. Neher, N. Koch, Y. Wu, V. M. Le Corre, H. Snaith, M. Stolterfoht, *Nat. Energy* **2024**, *9*, 664.
[29] N. Phung, A. Mattoni, J. A. Smith, D. Skroblin, H. Köbler, L. Choubrac, J. Breternitz, J. Li, T. Unold, S. Schorr, C. Gollwitzer, I. G. Scheblykin, E. L. Unger, M. Saliba, S. Meloni, A. Abate, A. Merdasa, *Joule* **2022**, *6*, 2152.
[30] B. P. Finkenauer, Akriti, K. Ma, L. Dou, *ACS Appl. Mater. Interfaces* **2022**, *14*, 24073.
[31] M. Othman, Q. Jeangros, D. A. Jacobs, M. H. Futscher, S. Zeiske, A. Armin, A. Jaffrès, A. G. Kuba, D. Chernyshov, S. Jenatsch, S. Züfle, B. Ruhstaller, S. Tabean, T. Wirtz, S. Eswara, J. Zhao, T. J. Savenije, C. Ballif, C. M. Wolff, A. Hessler-Wyser, *Energy Environ. Sci.* **2024**, *17*, 3832.
[32] S. Macpherson, T. A. S. Doherty, A. J. Winchester, S. Kosar, D. N. Johnstone, Y.-H. Chiang, K. Galkowski, M. Anaya, K. Frohna, A. N. Iqbal, S. Nagane, B. Roose, Z. Andaji-Garmaroudi, K. W. P. Orr, J. E. Parker, P. A. Midgley, K. M. Dani, S. D. Stranks, *Nature* **2022**, *607*, 294.
[33] L. Duan, D. Walter, N. Chang, J. Bullock, D. Kang, S. P. Phang, K. Weber, T. White, D. Macdonald, K. Catchpole, H. Shen, *Nat. Rev. Mater.* **2023**, *8*, 261.
[34] F. H. Isikgor, S. Zhumagali, L. V. T. Merino, M. De Bastiani, I. McCulloch, S. De Wolf, *Nat. Rev. Mater.* **2022**, *8*, 89.
[35] C. C. Boyd, R. Cheacharoen, K. A. Bush, R. Prasanna, T. Leijtens, M. D. McGehee, *ACS Energy Lett.* **2018**, *3*, 1772.
[36] S. Zhang, Z. Liu, W. Zhang, Z. Jiang, W. Chen, R. Chen, Y. Huang, Z. Yang, Y. Zhang, L. Han, W. Chen, *Adv. Energy Mater.* **2020**, *10*, 2001610.
[37] P. Schulz, D. Cahen, A. Kahn, *Chem. Rev.* **2019**, *119*, 3349.
[38] J. Xia, M. Sohail, M. K. Nazeeruddin, *Adv. Mater.* **2023**, *35*, 2211324.
[39] Q. C. Burlingame, Y.-L. Loo, E. A. Katz, *Nat. Energy* **2023**, *8*, 1300.
[40] Q. Jiang, R. Tirawat, R. A. Kerner, E. A. Gaulding, Y. Xian, X. Wang, J. M. Newkirk, Y. Yan, J. J. Berry, K. Zhu, *Nature* **2023**, *623*, 313.
[41] J. Li, J. Dagar, O. Shargaieva, O. Maus, M. Remec, Q. Emery, M. Khenkin, C. Ulbrich, F. Akhundova, J. A. Márquez, T. Unold, M. Fenske, C. Schultz, B. Stegemann, A. Al-Ashouri, S. Albrecht, A. T. Esteves, L. Korte, H. Köbler, A. Abate, D. M. Többens, I. Zizak, E. J. W. List-Kratochvil, R. Schlatmann, E. Unger, *Adv. Energy Mater.* **2023**, *13*, 2203898.
[42] J. Suo, B. Yang, E. Mosconi, D. Bogachuk, T. A. S. Doherty, K. Frohna, D. J. Kubicki, F. Fu, Y. Kim, O. Er-Raji, T. Zhang, L. Baldinelli, L.

Wagner, A. N. Tiwari, F. Gao, A. Hinsch, S. D. Stranks, F. De Angelis, A. Hagfeldt, *Nat. Energy* **2024**, *9*, 172.
[43] R. Azmi, E. Ugur, A. Seitkhan, F. Aljamaan, A. S. Subbiah, J. Liu, G. T. Harrison, M. I. Nugraha, M. K. Eswaran, M. Babics, Y. Chen, F. Xu, T. G. Allen, A. ur Rehman, C.-L. Wang, T. D. Anthopoulos, U. Schwingenschlögl, M. De Bastiani, E. Aydin, S. De Wolf, *Science* **2022**, *376*, 73.
[44] C. Liu, Y. Yang, H. Chen, J. Xu, A. Liu, A. S. R. Bati, H. Zhu, L. Grater, S. S. Hadke, C. Huang, V. K. Sangwan, T. Cai, D. Shin, L. X. Chen, M. C. Hersam, C. A. Mirkin, B. Chen, M. G. Kanatzidis, E. H. Sargent, *Science* **2023**, *382*, 810.
[45] J. Xu, H. Chen, L. Grater, C. Liu, Y. Yang, S. Teale, A. Maxwell, S. Mahesh, H. Wan, Y. Chang, B. Chen, B. Rehl, S. M. Park, M. G. Kanatzidis, E. H. Sargent, *Nat. Mater.* **2023**, *22*, 1507.
[46] I. L. Braly, D. W. deQuilettes, L. M. Pazos-Outón, S. Burke, M. E. Ziffer, D. S. Ginger, H. W. Hillhouse, *Nat. Photonics* **2018**, *12*, 355.
[47] J. Xu, C. C. Boyd, Z. J. Yu, A. F. Palmstrom, D. J. Witter, B. W. Larson, R. M. France, J. Werner, S. P. Harvey, E. J. Wolf, W. Weigand, S. Manzoor, M. F. A. M. van Hest, J. J. Berry, J. M. Luther, Z. C. Holman, M. D. McGehee, *Science* **2020**, *367*, 1097.
[48] F. Yang, P. Tockhorn, A. Musiienko, F. Lang, D. Menzel, R. Macqueen, E. Köhnen, K. Xu, S. Mariotti, D. Mantione, L. Merten, A. Hinderhofer, B. Li, D. R. Wargulski, S. P. Harvey, J. Zhang, F. Scheler, S. Berwig, M. Roß, J. Thiesbrummel, A. Al-Ashouri, K. O. Brinkmann, T. Riedl, F. Schreiber, D. Abou-Ras, H. Snaith, D. Neher, L. Korte, M. Stolterfoht, S. Albrecht, *Adv. Mater.* **2024**, *36*, 2307743.
[49] S. Tan, T. Huang, I. Yavuz, R. Wang, T. W. Yoon, M. Xu, Q. Xing, K. Park, D.-K. Lee, C.-H. Chen, R. Zheng, T. Yoon, Y. Zhao, H.-C. Wang, D. Meng, J. Xue, Y. J. Song, X. Pan, N.-G. Park, J.-W. Lee, Y. Yang, *Nature* **2022**, *605*, 268.
[50] A. A. Sutanto, P. Caprioglio, N. Drigo, Y. J. Hofstetter, I. Garcia-Benito, V. I. E. Queloz, D. Neher, M. K. Nazeeruddin, M. Stolterfoht, Y. Vaynzof, G. Grancini, *Chem* **2021**, *7*, 1903.
[51] D. B. Khadka, Y. Shirai, M. Yanagida, H. Ota, A. Lyalin, T. Taketsugu, K. Miyano, *Nat. Commun.* **2024**, *15*, 882.
[52] H. Kim, S.-M. Yoo, B. Ding, H. Kanda, N. Shibayama, M. A. Syzgantseva, F. F. Tirani, P. Schouwink, H. J. Yun, B. Son, Y. Ding, B.-S. Kim, Y. Y. Kim, J. Park, O. A. Syzgantseva, N. J. Jeon, P. J. Dyson, M. K. Nazeeruddin, *Nat. Commun.* **2024**, *15*, 5632.
[53] J. A. Steele, E. Solano, D. Hardy, D. Dayton, D. Ladd, K. White, P. Chen, J. Hou, H. Huang, R. A. Saha, L. Wang, F. Gao, J. Hofkens, M. B. J. Roeffaers, D. Chernyshov, M. F. Toney, *Adv. Energy Mater.* **2023**, *13*, 2300760.
[54] J. M. Hoffman, J. Strzalka, N. C. Flanders, I. Hadar, S. A. Cuthriell, Q. Zhang, R. D. Schaller, W. R. Dichtel, L. X. Chen, M. G. Kanatzidis, *Adv. Mater.* **2020**, *32*, 2002812.
[55] P. Cheng, P. Wang, Z. Xu, X. Jia, Q. Wei, N. Yuan, J. Ding, R. Li, G. Zhao, Y. Cheng, K. Zhao, S. F. Liu, *ACS Energy Lett.* **2019**, *4*, 1830.
[56] X. Huo, S. Mariotti, Y. Li, T. Guo, C. Ding, P. Ji, S. Yuan, T. Li, N. Meng, X. Liu, J. Zhang, I. N. Rabehi, Y. Zhang, S. Zhao, H. Wang, D. Song, L. K. Ono, Z. Xu, Y. Qi, *Energy Environ. Sci.* **2024**, *17*, 8658.
[57] J. Hu, P. Chen, D. Luo, L. Dai, N. Chen, S. Li, S. Yang, Z. Fu, D. Wang, Q. Gong, S. D. Stranks, R. Zhu, Z.-H. Lu, *Energy Environ. Sci.* **2022**, *15*, 5340.
[58] Y. Liu, H. Zhou, Y. Ni, J. Guo, R. Lu, C. Li, X. Guo, *Joule* **2023**, *7*, 1016.
[59] F. Li, X. Deng, F. Qi, Z. Li, D. Liu, D. Shen, M. Qin, S. Wu, F. Lin, S.-H. Jang, J. Zhang, X. Lu, D. Lei, C.-S. Lee, Z. Zhu, A. K.-Y. Jen, *J. Am. Chem. Soc.* **2020**, *142*, 20134.
[60] S. Tao, I. Schmidt, G. Brocks, J. Jiang, I. Tranca, K. Meerholz, S. Olthof, *Nat. Commun.* **2019**, *10*, 2560.
[61] D. Menzel, A. Tejada, A. Al-Ashouri, I. Levine, J. A. Guerra, B. Rech, S. Albrecht, L. Korte, *ACS Appl. Mater. Interfaces* **2021**, *13*, 43540.
[62] H. Hempel, T. J. Savenjie, M. Stolterfoht, J. Neu, M. Failla, V. C. Paingad, P. Kužel, E. J. Heilweil, J. A. Spies, M. Schleuning, J. Zhao, D. Friedrich, K. Schwarzburg, L. D. A. Siebbeles, P. Dörflinger, V. Dyakonov, R. Katoh, M. J. Hong, J. G. Labram, M. Monti, E. Butler-Caddle, J. Lloyd-Hughes, M. M. Taheri, J. B. Baxter, T. J. Magnanelli, S. Luo, J. M. Cardon, S. Ardo, T. Unold, *Adv. Energy Mater.* **2022**, *12*, 2102776.
[63] B. Krogmeier, F. Staub, D. Grabowski, U. Rau, T. Kirchartz, *Sustainable Energy Fuels* **2018**, *2*, 1027.
[64] Y. Yuan, G. Yan, C. Dreessen, T. Rudolph, M. Hülsbeck, B. Klingebiel, J. Ye, U. Rau, T. Kirchartz, *Nat. Mater.* **2024**, *23*, 391.
[65] I. Levine, A. Al-Ashouri, A. Musiienko, H. Hempel, A. Magomedov, A. Drevilkauskaite, V. Getautis, D. Menzel, K. Hinrichs, T. Unold, S. Albrecht, T. Dittrich, *Joule* **2021**, *5*, 2915.
[66] J. Pospisil, L. Marackova, O. Zmeskal, A. Kovalenko, *Appl. Phys. A.* **2023**, *129*, 129.
[67] S. Akel, A. Kulkarni, U. Rau, T. Kirchartz, *PRX Energy* **2023**, *2*, 013004.
[68] U. Aeberhard, S. Altazin, L. Stepanova, A. Stous, B. Blülle, C. Kirsch, E. Knapp, B. Ruhstaller, *IEEE Photovoltaic Spec. Conf.*, IEEE, Chicago, IL, USA, **2019**, pp. 0105–0111.
[69] Y. Zheng, Y. Li, R. Zhuang, X. Wu, C. Tian, A. Sun, C. Chen, Y. Guo, Y. Hua, K. Meng, K. Wu, C.-C. Chen, *Energy Environ. Sci.* **2023**, *17*, 1153.
[70] A. Gallastegui, G. Lingua, N. Lopez-Larrea, R. Carfora, D. Pasini, D. Mantione, D. Mecerreyes, *Macromol. Rapid Commun.* **2024**, *45*, 2400184.
[71] L. Krückemeier, Z. Liu, B. Krogmeier, U. Rau, T. Kirchartz, *Adv. Energy Mater.* **2021**, *11*, 2102290.
[72] Th. Dittrich, S. Bönisch, P. Zabel, S. Dube, *Rev. Sci. Instrum.* **2008**, *79*, 113903.
[73] S. P. Harvey, J. Messinger, K. Zhu, J. M. Luther, J. J. Berry, *Adv. Energy Mater.* **2020**, *10*, 1903674.
[74] I. Zizak, *J. large-Scale Res. Facilities* **2016**, *2*, A102.
[75] Z. Jiang, *J. Appl. Cryst.* **2015**, *48*, 917.
[76] H. Köbler, S. Neubert, M. Jankovec, B. Glažar, M. Haase, C. Hilbert, M. Topič, B. Rech, A. Abate, *Energy Technol.* **2022**, *10*, 2200234.
[77] L. Rakocevic, F. Ernst, N. T. Yimga, S. Vashishtha, T. Aernouts, T. Heumueller, C. J. Brabec, R. Gehlhaar, J. Poortmans, *Sol. RRL* **2019**, *3*, 1800287.
[78] J. Diekmann, P. Caprioglio, M. H. Futscher, V. M. Le Corre, S. Reichert, F. Jaiser, M. Arvind, L. P. Toro, E. Gutierrez-Partida, F. Peña-Camargo, C. Deibel, B. Ehrler, T. Unold, T. Kirchartz, D. Neher, M. Stolterfoht, *Sol. RRL* **2021**, *5*, 2100219.